

Flow of a gravity current in a porous medium accounting for drainage from a permeable substrate and an edge

Yingxian Estella Yu, Zhong Zheng,^{*} and Howard A. Stone[†]
*Department of Mechanical and Aerospace Engineering, Princeton University,
 Princeton, New Jersey 08544, USA*

(Received 6 September 2016; published 13 July 2017)

We study the coupled drainage mechanisms of a propagating viscous gravity current that leaks fluid through a permeable substrate and a fixed edge. Using both theoretical analyses and numerical simulations, we investigate the time evolution of the profile shape and the amount of fluid loss through each of the drainage mechanisms. For the case of a finite-volume release, asymptotic solutions are provided to describe the dynamics of the profile shapes. Specifically, for the case of buoyancy-driven drainage with finite-volume release, an early-time self-similar solution is obtained to describe the profile evolution and a late-time self-similar solution is approached in the limit of pure edge drainage. For the case of constant fluid injection, numerical and analytical solutions are given to describe the time evolution and the steady-state profile shapes, as well as the partition of the fluid loss through each mechanism. We also briefly discuss the practical implications of the theoretical predictions to the CO₂ sequestration and leakage problems.

DOI: [10.1103/PhysRevFluids.2.074101](https://doi.org/10.1103/PhysRevFluids.2.074101)

I. INTRODUCTION

Gravity currents occur when a fluid of one density flows into another fluid of a different density, with the flow velocity primarily parallel to the base. Typical examples of gravity currents can be found, for example, in lava flows, sea breeze fronts, propagating dust storms, and leakage of viscous fluids from containers. In this work we are interested in viscous gravity currents in porous media, where inertial effects are negligible. A typical example arises in carbon dioxide (CO₂) sequestration, where supercritical CO₂ is injected into a porous reservoir and spreads through the porous medium because of buoyancy [1–9]. Other examples include fluid exchange and displacement in an oil reservoir [10,11], fluid transport in a horizontal channel [12–14], and underground water injection for seasonal heat storage [15].

Many investigations mentioned above assume that the gravity current is flowing on top of an impermeable substrate. Nevertheless, recent studies have focused on the case where leakage of the current is included during the propagation, as inspired by practical concerns, such as CO₂ leakage from subsurface sequestration projects (see, e.g., Refs. [16,17]). For example, a viscous gravity current with leakage through a thin permeable base is sketched in Fig. 1(a) (see, e.g., see Refs. [18–20], where distributed leakage is considered). Also, several studies have investigated the localized leakage of a gravity current through a fixed edge or a deep fracture in the substrate, as shown in Fig. 1(b) (see, e.g., see Refs. [17,20–24]). Other drainage mechanisms are possible including localized sinks [25], line sinks [26], drainage in vertical fractures [27], drainage in deep porous substrates [28,29], and drainage that includes capillary effects [30,31].

Another practical concern arises when multiple drainage mechanisms occur simultaneously. For example, Pritchard studied the steady-state profile solutions for gravity currents with coupled drainage due to distributed substrate drainage and leakage through deep localized fractures under

^{*}Present address: Department of Applied Mathematics and Theoretical Physics, University of Cambridge, Cambridge, United Kingdom.

[†]hastone@princeton.edu

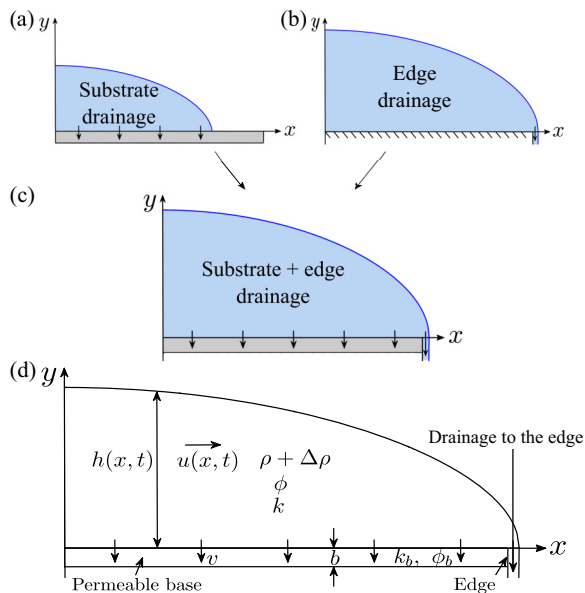


FIG. 1. Schematics of the coupled drainage problem, showing the typical profile shapes for a viscous gravity current flowing in configurations where leakage occurs. (a) When there is no drainage from an edge, the current will completely drain from the base. (b) When the substrate is impermeable, fluid can only drain from the edge. (c) When the current overshoots a permeable base with a fixed length scale, the fluid drains from both the permeable base and the edge. (d) Schematics of fluid drainage from both a permeable base and a fixed edge, with mechanical properties of interest labeled.

constant fluid injection [16]. In this paper we are interested in the coupled drainage effects of a permeable substrate and a fixed edge [Fig. 1(c)], which can occur due to a finite length of the permeable caprock in the case of CO_2 sequestration. We investigate the temporal evolution of the gravity current profile with coupled drainage effects, especially under a finite-volume release. We also seek to explore how the competition of these two mechanisms will change the gravity current profiles and the amount of fluid loss.

In addition, based on the different vertical drainage velocities through a permeable base, our analysis can be further categorized in two ways: The first is when the drainage is due to gravity and the other is when the drainage is due to externally imposed effects, such as dissolution-driven convection [4]. The former involves a heterogeneous drainage velocity along the horizontal coordinate, depending, for example, on the local height of the current, as will be discussed in Sec. II A. The analysis will be followed by a discussion of a uniform current drainage in Sec. II B, which is associated with an externally imposed, homogeneous, and constant vertical drainage velocity through the permeable substrate. In each section, the cases of both finite-volume release and constant injection flow rate will be considered and each is studied with both theoretical analyses and numerical calculations. Practical implications for CO_2 leakage from geological sequestration projects will be discussed in Sec. III.

II. THEORY

In this paper we consider the motion of a gravity current in a semi-infinite porous medium, where the fluid can drain from both a permeable substrate and a fixed edge [Fig. 1(c)]. We assume that the porous medium is homogeneous with permeability k and porosity ϕ and is filled with an ambient fluid of constant density ρ . Fluid with density difference $\Delta\rho$ with the ambient fluid and viscosity μ flows

above a permeable base, which has a small thickness b , permeability k_b ($k_b \ll k$), and porosity ϕ_b . A vertical flow velocity $v(x,t)$ is included to describe the effect of drainage through the permeable substrate. In addition, a finite horizontal length scale L is imposed so that the buoyancy-driven current will drain from the edge beyond this distance [Fig. 1(d)]. The shape of the current $h(x,t)$ is assumed to satisfy $|\partial h/\partial x| \ll 1$ [1,32] and is described by the one-dimensional continuity equation

$$\phi \frac{\partial h}{\partial t} + \frac{\partial}{\partial x}(uh) = -v, \quad (1)$$

where $u(x,t)$ represents the horizontal Darcy velocity and $v(x,t) > 0$ is the vertical Darcy velocity draining through the permeable substrate. The horizontal velocity $u(x,t)$ is described by Darcy flow due to hydrostatic pressure and is sometimes referred to as the Dupuit approximation [33]

$$u = -\frac{\Delta\rho g k}{\mu} \frac{\partial h}{\partial x}. \quad (2)$$

A. Buoyancy-driven drainage

In this section we assume that the vertical flow is driven by buoyancy effects such that the vertical flow velocity $v(x,t)$ is given by

$$v \approx \frac{\Delta\rho g k_b h}{\mu b}. \quad (3)$$

Note that Eq. (3) has been employed in several previous studies that have considered drainage through a permeable substrate [16,18,25,34] and this approximation is only valid with the assumption that $h \gg b$. By substituting Eqs. (2) and (3) into (1), the evolution equation for the profile shape $h(x,t)$ can be rewritten as

$$\frac{\phi\mu}{\Delta\rho g k} \frac{\partial h}{\partial t} = \frac{\partial}{\partial x} \left(h \frac{\partial h}{\partial x} \right) - \frac{k_b h}{kb}, \quad (4)$$

which is the starting point for our analysis.

1. Finite volume

We first consider the sudden release of a fluid with a finite volume. We assume that the substrate has a fixed length L and $x = L$ represents the location of the edge. Here we consider a rectangular profile with a finite volume $V = h_0 L$, which initially fills the domain $0 \leq x \leq L$:

$$h(x,0) = \begin{cases} h_0, & 0 \leq x \leq L \\ 0, & x > L. \end{cases} \quad (5)$$

The velocity at the origin is zero $u(0,t) = 0$ due to symmetry. Therefore, we impose a no-flux boundary condition at the origin $x = 0$ according to Eq. (2). We also assume that the current height at the edge $x = L$ is zero for all time. Thus, we obtain two boundary conditions

$$\left. \frac{\partial h}{\partial x} \right|_{x=0} = 0, \quad h(L,t) = 0, \quad (6)$$

which are the same as those in the case of pure edge drainage [20]. Note that in practice, we used a tanh function in numerical simulations to approximate the rectangular profile (5) so that the initial condition is smooth in the entire domain $0 \leq x \leq L$. Thus the near-rectangular initial condition and the boundary condition $h(L,t) = 0$ are consistent at the edge $x = L$ and the profile is rapidly smoothed for $\hat{t} > 0$. Dimensionless variables can then be defined as

$$\hat{x} \equiv \frac{x}{L}, \quad \hat{h} \equiv \frac{h}{h_0}, \quad \hat{t} \equiv \frac{t\Delta\rho g k h_0}{\phi\mu L^2}, \quad (7)$$

so that the governing equation (4) and the initial and boundary conditions (5) and (6) become

$$\frac{\partial \hat{h}}{\partial \hat{t}} = \frac{\partial}{\partial \hat{x}} \left(\hat{h} \frac{\partial \hat{h}}{\partial \hat{x}} \right) - \lambda \hat{h}, \quad (8a)$$

$$\hat{h}(\hat{x}, 0) = \begin{cases} 1, & 0 \leq \hat{x} \leq 1 \\ 0, & \hat{x} > 1, \end{cases} \quad (8b)$$

$$\left. \frac{\partial \hat{h}}{\partial \hat{x}} \right|_{\hat{x}=0} = 0, \quad \hat{h}(1, \hat{t}) = 0, \quad (8c)$$

where

$$\lambda \equiv \frac{k_b L^2}{k b h_0} \quad (9)$$

is a dimensionless parameter that measures the resistance for the gravity current to drain through the permeable substrate relative to flowing through the porous medium.

We performed numerical simulations to solve Eq. (8a), subject to initial condition (8b) and boundary conditions (8c). More details about the numerical schemes are provided in the Appendix. After a finite volume of fluid is released, as shown in Fig. 2(a), the current drains from both the edge and the permeable bed and the front of the current remains pinned at the fixed edge $\hat{x} = 1$. In addition, the profiles at both the early and late times inspire us to seek self-similar solutions.

To begin with, we note that Eq. (8a) can be further simplified by using the substitutions [18,20,35] to eliminate the dependence on λ :

$$H(\hat{x}, \tau) = \hat{h}(\hat{x}, \hat{t}) \exp(\lambda \hat{t}), \quad \tau = \frac{1 - \exp(-\lambda \hat{t})}{\lambda}. \quad (10)$$

Substituting (10) into (8) and (9) yields an evolution equation for $H(\hat{x}, \tau)$, as well as the initial and boundary conditions

$$\frac{\partial H}{\partial \tau} = \frac{\partial}{\partial \hat{x}} \left(H \frac{\partial H}{\partial \hat{x}} \right), \quad (11a)$$

$$H(\hat{x}, 0) = \begin{cases} 1, & 0 \leq \hat{x} \leq 1 \\ 0, & \hat{x} > 1, \end{cases} \quad (11b)$$

$$\left. \frac{\partial H}{\partial \hat{x}} \right|_{\hat{x}=0} = 0, \quad H(1, \tau) = 0. \quad (11c)$$

The boundary-initial value problems (BIVPs) (11) and (8) are equivalent. By suppressing λ , the BIVP (11) takes the same form as the case of pure edge drainage [20]. Nevertheless, τ is only defined in the domain $0 \leq \tau < 1/\lambda$ based on the transformation (10).

In the specific case of a rectangular initial condition, the rescaled gravity current height at the origin $H(0, \tau)$ remains as unity at early times before the information of the edge reaches the origin, which can further restrict the Neumann condition $\frac{\partial H}{\partial \hat{x}}(0, \tau) = 0$ in the boundary condition (11c) to a Dirichlet condition

$$H(0, \tau) = 1. \quad (12)$$

Thus, a scaling analysis can be performed and the form of the partial differential equation (PDE) (11a) suggests that the early-time self-similar solution is in the form

$$H(\hat{x}, \tau) = \psi(\eta), \quad \eta = \frac{\hat{x} - 1}{\sqrt{2\tau}}, \quad (13)$$

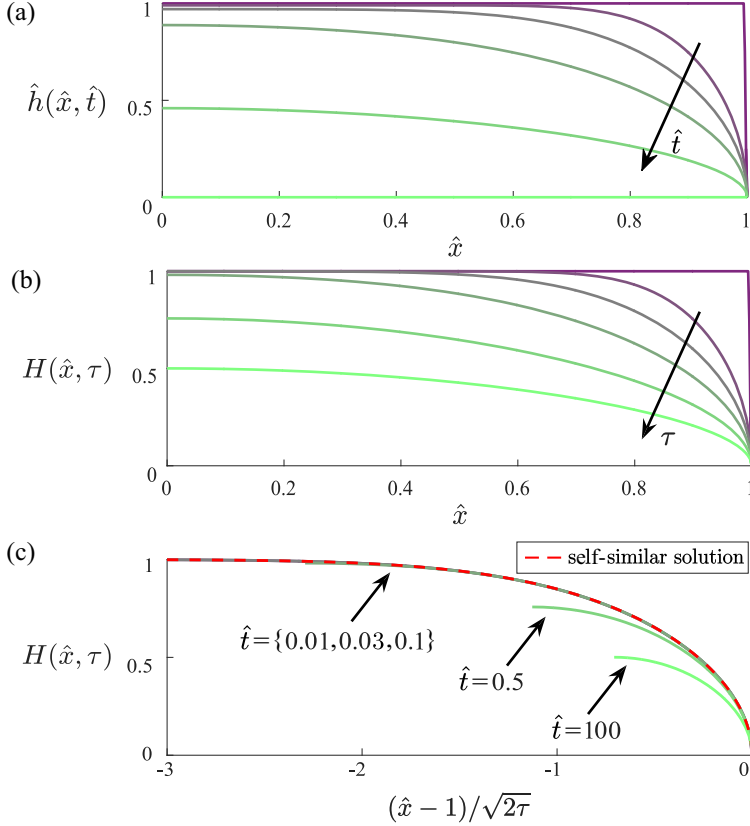


FIG. 2. Time evolution profiles of a gravity current draining from an edge for typical values of λ and the early-time self-similar solution. (a) Profile evolution $\hat{h}(\hat{x}, \hat{t})$ for $\lambda = 1$ at $\hat{t} = \{0, 0.01, 0.03, 0.1, 0.5, 100\}$. The initial condition is a rectangular profile (8b). (b) Gravity current profile evolution for $\lambda = 1$ shown as the transformed height $H(\hat{x}, \tau)$, where τ represents the transformed time. The information of the edge has not reached the origin and $H(0, \tau) = 1$ before $\hat{t} = 0.5$ (or $\tau = 0.39$). (c) Rescaled numerical solutions for $\lambda = 1$ at different times $\hat{t} = \{0, 0.01, 0.03, 0.1, 0.5, 100\}$. The early-time self-similar solution is shown as the red dashed curve, which agrees well with the rescaled profiles at times $\hat{t} = \{0, 0.01, 0.03, 0.1\}$ (or $\tau = \{0, 0.01, 0.03, 0.1\}$). The rescaled profiles deviate from the early-time self-similar profile at $\hat{t} = \{0.5, 100\}$ (or $\tau = \{0.39, 1.0\}$), since the boundary condition $H(0, \tau) = 1$ does not hold anymore after the information from the edge has reached the origin.

where $\psi(\eta)$ is the early-time self-similar profile and η is the similarity variable. We expect that this self-similar profile is approached before the information at the edge reaches the origin. Substituting (13) into (11), we obtain

$$(\psi\psi')' + \eta\psi' = 0 \quad \text{with } \psi(-\infty) = 1, \psi(0) = 0, \quad (14)$$

which applies to any λ . The transformed profile evolution in time $H(\hat{x}, \tau)$ for $\lambda = 1$ is shown in Fig. 2(b), where the edge information is still propagating towards the origin at times $\hat{t} = \{0.01, 0.03, 0.1\}$. The gravity current profiles are rescaled and shown in Fig. 2(c), where the rescaled profiles at times $\hat{t} = \{0.01, 0.03, 0.1\}$ overlap one another and agree well with the early-time self-similar solution (red dashed curve). After the information has reached the origin, the height at the origin cannot be assumed to be $H(0, \tau) = 1$ anymore. Thus, the scaling shown in Eq. (13) fails beyond this time scale and the rescaled profiles deviate from the early-time self-similar solution, as shown in Fig. 2(c) for times $\hat{t} = \{0.5, 100\}$.

As time progresses, the assumption $H(0, \tau) = 1$ eventually fails and the early-time self-similar solution no longer captures the gravity current profile evolution. At long times, however, Eq. (11) can be rescaled differently, which leads to a late-time self-similar solution. As is well known, the nonlinear PDE (11a) can be further reduced to a nonlinear ordinary differential equation via steps inspired by scaling arguments. Since the substrate length scale L is a constant, the form of Eq. (11a) and boundary conditions (11c) suggest that a late-time self-similar solution is given by

$$H(\hat{x}, \tau) = \frac{f(\hat{x})}{\tau}, \quad (15)$$

where $f(\hat{x})$ represents the universal profile shape. This universal profile solution will be approached at the transformed time limit $\tau \rightarrow \infty$, which can only be achieved for $\lambda \rightarrow 0$. With Eq. (15), the PDE (11a) as well as its boundary conditions (11c) can be reduced to a boundary value problem (BVP) for the ordinary differential equation (ODE)

$$(ff')' + f = 0 \quad \text{with} \quad f'(0) = 0, \quad f(1) = 0, \quad (16)$$

whose solution is the late-time self-similar solution. At the limit $\lambda \rightarrow 0$, the BVP (16) is identical to that in pure edge drainage [20], in which (16) is solved numerically.

Notice that as time $\hat{t} \rightarrow \infty$, the transformed time $\tau \rightarrow 1/\lambda$ and therefore the gravity current profile approaches the solution to Eq. (11) evaluated at $\tau = 1/\lambda$. As a result, there are two different late-time asymptotic limits in this coupled drainage problem: a numerical solution to Eq. (8) or (11) as $\hat{t} \rightarrow \infty$, which provides the final profile shape of the gravity current, and a self-similar solution as $\tau \rightarrow \infty$, which can be approached only at the limit $\lambda \rightarrow 0$. The value of λ determines the extent to which the numerical solution approaches the self-similar solution. In the following context, the discussion of the self-similar solution $\tau \rightarrow \infty$ ($\lambda \rightarrow 0$) will be provided first, followed by a discussion of the numerical solution with finite values of λ .

To start, we solve for the late-time self-similar solution analytically. After multiplying by ff' and integrating once, Eq. (16) reduces to

$$(ff')^2 + \frac{2}{3}[f^3 - f(0)^3] = 0 \quad \text{with} \quad f(1) = 0, \quad (17)$$

which can be further simplified, by defining $\chi \equiv f/f(0)$, to

$$\chi' = -\left(\frac{2}{3f(0)}\right)^{1/2} \frac{(1 - \chi^3)^{1/2}}{\chi} \quad \text{with} \quad \chi(1) = 0. \quad (18)$$

After integration using *Mathematica*, the self-similar solution can be expressed in terms of the hypergeometric function ${}_2F_1$:

$${}_2F_1\left(\frac{1}{2}, \frac{2}{3}; \frac{5}{3}; \chi^3\right) \chi^2 = \left(\frac{8}{3f(0)}\right)^{1/2} (1 - \hat{x}). \quad (19)$$

The value of $f(0)$ can be obtained by applying the condition $\chi(0) = 1$, which gives

$$f(0) = \frac{8\Gamma(7/6)^2}{3\pi\Gamma(5/3)^2} = 0.8964, \quad (20)$$

with Γ representing the Gamma function. A numerical shooting procedure is also performed using the MATLAB subroutine ODE45 in order to solve Eq. (16), with $\lambda = 10^{-5}$ and $f(0) = 0.8964$. The numerically solved self-similar solution is found to agree with the analytical solution (19). Therefore, the analytical solution (19) is shown in the figures as the late-time self-similar solution in the remainder of this section. The time evolution for the gravity current with $\lambda = 10^{-5}$ is shown in Fig. 3(a), whose results are further rescaled and shown in Fig. 3(b), along with the self-similar solution (19) (blue dashed curve) as a comparison. Note that for the limit $\lambda \rightarrow 0$, the transformed time $\tau \rightarrow \infty$ as $\hat{t} \rightarrow \infty$; therefore, the numerical PDE solution as $\hat{t} \rightarrow \infty$ is equivalent to the late-time self-similar solution. As time progresses, the rescaled profiles $\tau H(\hat{x}, \tau)$ shown in Fig. 3(b)

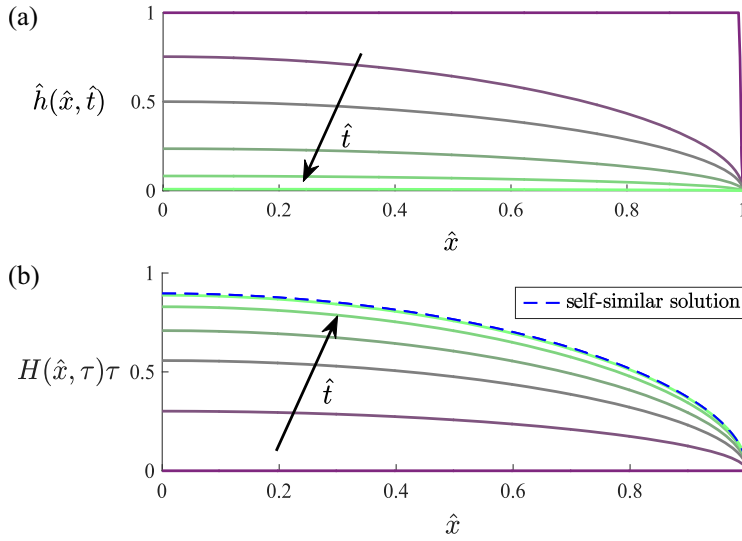


FIG. 3. Gravity current profile evolution for a finite-volume release. Numerical results for the evolution of the gravity current with time, with $\lambda = 10^{-5}$, $\hat{t} = \{0, 0.4, 1, 3, 10, 100\}$, starting from an initial rectangular profile (8b). The shapes of the gravity current are marked with colors varying from purple to green as the simulation time progresses to larger values. (a) Numerical results showing the current changes with time. (b) Rescaled profiles from (a), along with a comparison with the theoretically predicted solution profile (blue dashed curve) obtained from Eq. (16). As time progresses, the rescaled profile approaches the self-similar shape.

approach a universal shape, which agrees with the theoretical prediction of the self-similar solution. For example, at $\hat{t} = 100$, the value of $\tau H(0, \tau)$ reaches 0.8850, which is within 1% of the theoretical value $f(0) = 0.8964$. In addition, the initial fluid profile only affects the early-time current shapes before the self-similar behavior is established. Thus, the initial fluid shape is not limited to the rectangular profile chosen here.

As mentioned above, a finite value of λ corresponds to a finite upper bound for the transformed time $\tau = 1/\lambda$. Therefore, with an increase of the value of λ , it is expected that the numerical solution ($\hat{t} \rightarrow \infty$) will deviate from the self-similar solution. The gravity current profile evolution for $\lambda = 1$ is shown in Fig. 4(a). As time $\hat{t} \rightarrow \infty$, the rescaled profile shapes resemble a similarity profile, which corresponds to the solution of Eq. (11) as time $\tau \rightarrow 1/\lambda$. However, limited by the upper bound of τ , the transformed time τ is not large enough for the numerical solution to converge to the self-similar solution (19) and disagreement between the numerical solution and the self-similar solution is shown (for $\lambda = 1$). The effect of λ on the numerical solution as $\hat{t} \rightarrow \infty$ is shown in Fig. 4(b), where the rescaled numerical solutions at different values of λ are displayed. The self-similar solution (19) (red dashed curve) is also displayed for comparison. As the value of λ increases, the rescaled numerical solution deviates from the self-similar solution to a larger extent and the maximum deviation has reached 7% at $\lambda = 0.1$. As a result, for large values of λ , the solution to the reduced equation (16) cannot provide an accurate prediction to the final gravity current shape and solving Eq. (8) or (11) is required.

It should also be pointed out that the numerical solutions corresponding to large values of λ can become sensitive to the initial conditions. The upper bound for τ decreases with the increasing value of λ , meaning that the transformed time may not be long enough to avoid the effect of the initial condition. As shown in Fig. 4(c), the rescaled numerical solutions evolved from different initial conditions are compared for $\lambda = 10^{-5}$ and $\lambda = 1$, respectively. The rescaled numerical solutions overlap one another at $\hat{t} = 100$ for $\lambda = 10^{-5}$, since the numerical solution as $\hat{t} \rightarrow \infty$ at the limit of $\lambda \rightarrow 0$ is equivalent to the self-similar solution. The rescaled numerical solutions for $\lambda = 1$, on

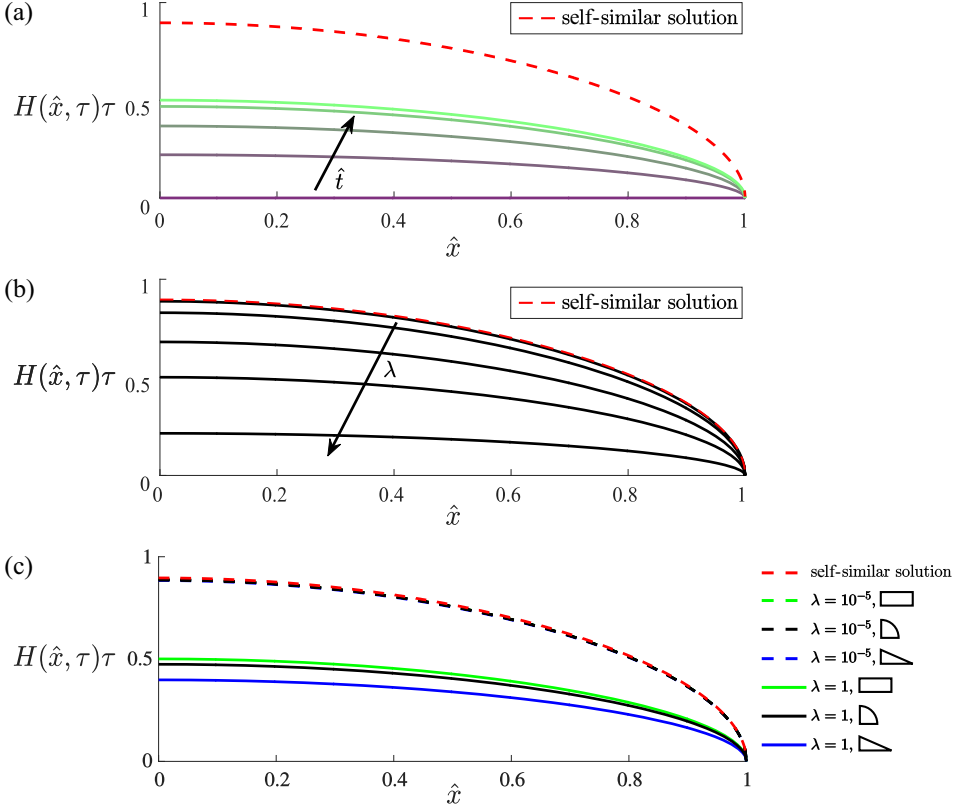


FIG. 4. Numerical solutions for typical values of λ . (a) Rescaled profile evolution for $\lambda = 1$ at $\hat{t} = \{0, 0.3, 0.8, 2, 100\}$. Initial condition is a rectangular profile (8b). The numerical solution as $\hat{t} \rightarrow \infty$ disagrees with the self-similar solution (red dashed curve) due to the finite value of $\tau = 1/\lambda = 1$. (b) Rescaled numerical solutions at different values of $\lambda = \{10^{-5}, 0.1, 0.4, 1, 4\}$ at time $\hat{t} = 100$. The black solid curves are the rescaled numerical results from solving the Eq. (8), starting from a rectangular initial profile (8b). As the value of λ increases, the numerical solution deviates more from the self-similar solution. (c) Initial condition dependence of the numerical solutions for a general λ . The rescaled numerical solutions with different initial conditions are compared for $\lambda = 10^{-5}$ (dashed curves) and $\lambda = 1$ (solid curves), respectively. The rectangular, quarter-circular, and triangular shapes in the legend represent the corresponding initial shapes of the gravity current. Green curves correspond to the rectangular initial condition (8b), black curves correspond to the quarter-unit-circle initial condition, and blue curves correspond to the triangular initial condition with $\hat{h}(0) = 1$ and $\hat{h}(1) = 0$. While the rescaled numerical solutions for $\lambda = 10^{-5}$ overlap one another and agree with the self-similar solution, the rescaled numerical solutions for $\lambda = 1$ with different initial conditions differ from one another and deviate from the self-similar solution.

the other hand, differ from one another depending on the initial conditions and disagree with the self-similar solution.

The fluid volume remaining in the porous medium is a quantity of practical interest and it is defined as

$$\hat{V}(\hat{t}) \equiv \int_0^1 \hat{h}(\hat{x}, \hat{t}) d\hat{x}. \quad (21)$$

Due to the solution's initial condition dependence, the value of $\hat{V}(\hat{t})$ for a general λ needs to be solved numerically. However, in the limit $\lambda \rightarrow 0$, the value of $\hat{V}(\hat{t})$ can be obtained analytically. In

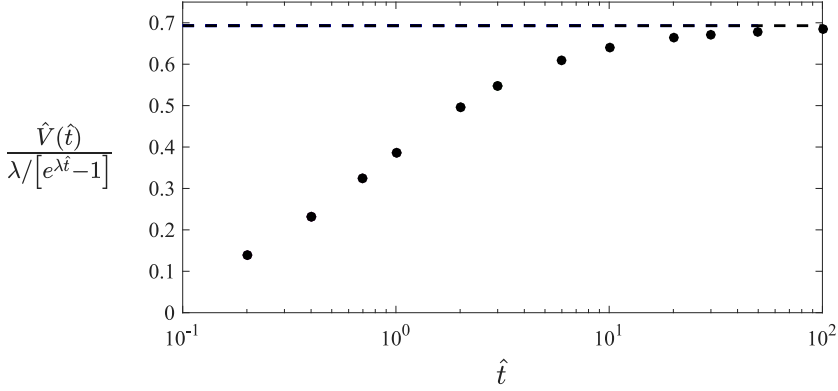


FIG. 5. Rescaled nondimensional volume remaining in the reservoir at the limit $\lambda \rightarrow 0$, calculated with a representative value of $\lambda = 10^{-5}$, at times $\hat{t} = \{0.1, 0.2, 0.4, 0.7, 1, 3, 6, 20, 30, 50, 100\}$. As time increases, the volume approaches a constant 0.6930, which is predicted by the self-similar solution $\int_0^1 f(\hat{x})d\hat{x}$ [see Eq. (21)]. The rescaled nondimensional volume reaches 0.6802 at $\hat{t} = 100$, which is within 2% of the theoretical prediction.

this limit, we can substitute Eqs. (10) and (15) into the definition of $\hat{V}(\hat{t})$ (21) and obtain

$$\hat{V}(\hat{t}) = \frac{\lambda}{\exp(\lambda\hat{t}) - 1} \int_0^1 f(\hat{x})d\hat{x}, \quad (22)$$

where $\int_0^1 f(\hat{x})d\hat{x} = 0.6930$ is a constant determined from the numerical computation, which represents the area enclosed between the self-similar profile (19) and the axes. Note that the volume described in Eq. (22) is valid only after the universal profile shape is established. The evolution of $\hat{V}(\hat{t})$ with time is shown in Fig. 5. As time progresses, the value of $\hat{V}(\hat{t})[\exp(\lambda\hat{t}) - 1]/\lambda$ approaches the theoretically predicted constant 0.6930.

Since both the fixed edge and the underlying permeable substrate are sources of fluid drainage, we are also interested in the amount of fluid loss due to each of the mechanisms in the limit of $\lambda \rightarrow 0$. The flux \hat{q}_{bed} draining through the permeable bed per unit width of the current is given by

$$\hat{q}_{\text{bed}}(t) = \int_0^1 \lambda \hat{h}(\hat{x}, t) d\hat{x} = \lambda \hat{V}(\hat{t}). \quad (23)$$

The total flux $\hat{q}(\hat{t})$ of the fluid drainage is

$$\hat{q}(\hat{t}) \equiv -\frac{d\hat{V}}{d\hat{t}} = \frac{\lambda \exp(\lambda\hat{t})}{\exp(\lambda\hat{t}) - 1} \hat{V}(\hat{t}). \quad (24)$$

Thus, the drainage fraction from the edge $\alpha \equiv \hat{q}_{\text{edge}}/\hat{q}$ can be expressed as

$$\alpha = \exp(-\lambda\hat{t}). \quad (25)$$

This result is also validated from the numerical calculations, as shown in Fig. 6, and the results show good agreement with Eq. (25). Note that the difference between the numerical simulation and the theoretical prediction decreases in time and the error is already within 6% at time $\hat{t} = 0.1$.

2. Constant injection rate

If there is a continuous supply of fluid with a constant flow rate q at the origin $x = 0$, the current will gradually evolve to a steady state for which the constant injection rate q equals the total drainage

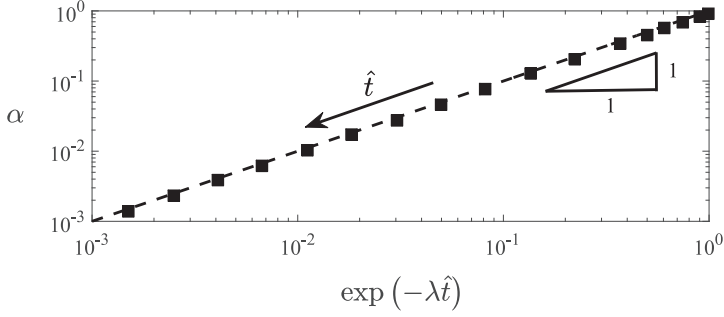


FIG. 6. Numerical results showing the drainage fraction α [Eq. (25)] variation with time, with $\lambda = 10^{-1}$, at times $\hat{t} = \{0.1, 1, 3, 5, 7, 10, 15, 20, 25, 30, 35, 40, 45, 50, 55, 60, 65\}$. The black dashed line represents the theoretical prediction $\alpha = \exp(-\lambda \hat{t})$. Note that the difference between the numerical simulation and the theoretical prediction decreases in time and the error is already within 6% at time $\hat{t} = 0.1$.

rate. While the governing equation remains (4), the initial and boundary conditions become

$$h(x, 0) = 0, \quad (26a)$$

$$h \frac{\partial h}{\partial x} \Big|_{x=0} = -\frac{q\phi\mu}{\Delta\rho gk}, \quad h(L, t) = 0. \quad (26b)$$

According to boundary conditions (26b), we can determine a characteristic length scale for the current height $h_c = (qL\phi\mu/\Delta\rho gk)^{1/2}$, which is related to the injection rate q . Next we define the dimensionless variables as

$$\hat{x} \equiv \frac{x}{L}, \quad \hat{h} \equiv h \left(\frac{\Delta\rho gk}{qL\phi\mu} \right)^{1/2}, \quad \hat{t} \equiv t \left(\frac{q\Delta\rho gk}{L^3\phi\mu} \right)^{1/2}, \quad (27)$$

which provide the dimensionless governing equation, as well as the initial and boundary conditions

$$\frac{\partial \hat{h}}{\partial \hat{t}} = \frac{\partial}{\partial \hat{x}} \left(\hat{h} \frac{\partial \hat{h}}{\partial \hat{x}} \right) - \lambda_q \hat{h}, \quad (28a)$$

$$\hat{h}(\hat{x}, 0) = 0, \quad (28b)$$

$$\hat{h} \frac{\partial \hat{h}}{\partial \hat{x}} \Big|_{\hat{x}=0} = -1, \quad \hat{h}|_{\hat{x}=1} = 0. \quad (28c)$$

Here λ_q is defined as

$$\lambda_q \equiv \frac{k_b L}{kb} \left(\frac{\Delta\rho gkL}{\phi\mu q} \right)^{1/2}, \quad (29)$$

which is related to the competition between the drainage and the injection rates.

Using a finite-difference scheme to solve the PDE (28a) with its initial and boundary conditions (28b) and (28c) (see the Appendix), we can obtain different current shape evolutions, depending on the values of λ_q . Figure 7 presents three typical time evolutions for $\lambda_q = 10^{-5}$, 2, and 10. As time progresses, the gravity current gradually evolves to its steady-state profile, where color is used to display the time evolution. The profile corresponding to the latest time shown in each plot represents the profile shape when a steady state is reached.

At the steady state, the constant injection flow rate is balanced by the total drainage rate, from both the permeable base and the edge, though the gravity current may only occupy $0 \leq \hat{x} \leq \hat{x}_f \leq 1$, where \hat{x}_f denotes the front of the gravity current. The steady-state governing equation and its

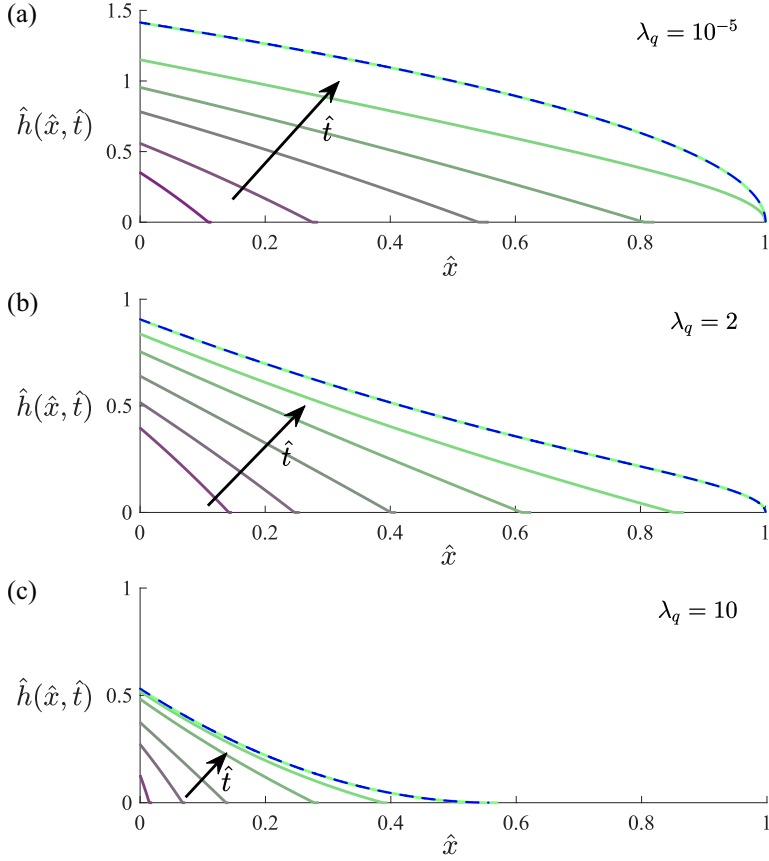


FIG. 7. Buoyancy-driven drainage gravity current profile evolutions with constant injection flow rate. The PDE solutions are shown at different λ_q values with a constant injection rate $\hat{h} \frac{\partial \hat{h}}{\partial \hat{x}} = -1$ at the origin. As time progresses, the current gradually evolves to its steady-state profile, whose color has gradually evolved to green. The corresponding solution to the reduced equation (30) is also shown as the blue dashed curves in each case as a comparison: (a) $\lambda_q = 10^{-5}$, the gravity current overshoots the edge, for times $\hat{t} = \{0.02, 0.08, 0.22, 0.4, 0.7, 10\}$; (b) $\lambda_q = 2$, the gravity current overshoots the edge, for times $\hat{t} = \{0.01, 0.03, 0.07, 0.15, 0.3, 0.55, 10\}$; and (c) $\lambda_q = 10$, the gravity current drains only from the permeable base for times $\hat{t} = \{10^{-3}, 0.02, 0.03, 0.1, 0.2, 1\}$.

boundary conditions can be rewritten as

$$\frac{d^2 \hat{h}_s^2}{d\hat{x}^2} = 2\lambda_q \hat{h}_s, \quad (30a)$$

$$\hat{h}_s \left. \frac{d\hat{h}_s}{d\hat{x}} \right|_{\hat{x}=0} = -1, \quad \hat{h}_s(\hat{x}_f) = 0, \quad (30b)$$

where $\hat{h}_s(\hat{x})$ represents the steady-state profile shape. When the front of the gravity current does not reach the fixed end ($\hat{x}_f < 1$), the extra information regarding the location of the leaking edge \hat{x}_f can be obtained from

$$\lambda_q \int_0^{\hat{x}_f} \hat{h}_s(\hat{x}) d\hat{x} = 1, \quad (31)$$

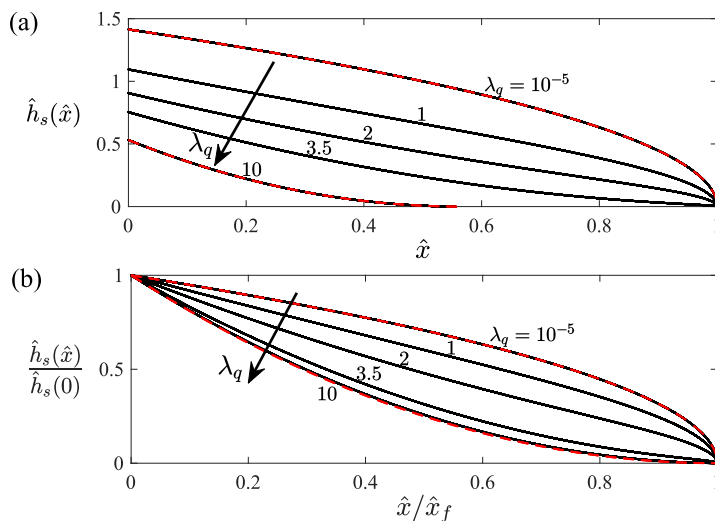


FIG. 8. Under constant flow rate fluid injection, steady-state profile variation with different values of λ_q . (a) Steady-state shapes variation with $\lambda_q = \{10^{-5}, 1, 2, 3.5, 10\}$. Numerical results are obtained from solving the ODE (30a) subject to boundary conditions (30b) and show good agreement with the analytical solutions (34) and (35) at the limits $\lambda_q > 3\sqrt{2}$ (i.e., $\hat{x}_f < 1$) (from Refs. [16,18]) and $\lambda_q \rightarrow 0$ (from Refs. [16,23,33]), which are shown as red dashed curves. (b) Rescaled steady-state profiles in (a). As the value of λ_q increases, the steady-state profile shape changes from a convex shape to a concave shape.

which indicates that the total drainage rate from the permeable substrate is balanced by the continuous fluid supply at the origin $\hat{x} = 0$. Given a value of λ_q , Eq. (30a) can be solved numerically, subject to the boundary conditions (30b) and (31). We used a shooting procedure with the MATLAB subroutine ODE45 and the corresponding solutions to Eq. (30) are shown as blue dashed curves in Fig. 7, where the solutions obtained from the PDE and ODE show good agreement. The solutions to the reduced equation (30) with different λ_q values are also shown in Fig. 8. As the value of λ_q increases, the steady-state profile varies from concave curves to convex curves.

To obtain more analytic insights, we integrate Eq. (30a) once to find

$$\frac{d\hat{h}_s^2}{d\hat{x}} = -\left(\frac{8}{3}\lambda_q\hat{h}_s^3 + c\right)^{1/2}, \quad (32)$$

where c is a non-negative integration constant, whose value is related to the drainage flux at the current tip, or the current height at the origin:

$$c = \left(\frac{d\hat{h}_s^2}{d\hat{x}}\Big|_{\hat{x}=\hat{x}_f}\right)^2 \quad \text{or} \quad c = 4 - \frac{8}{3}\lambda_q\hat{h}_s^3(0). \quad (33)$$

In particular, when λ_q is large enough, the gravity current will only drain from the permeable substrate. Therefore, at the front \hat{x}_f , the drainage flux $\sqrt{c}/2$ is zero. Thus, Eq. (32) can be simplified and solved with the flux boundary conditions (30b). The analytical solution in this case is

$$\hat{h}_s(\hat{x}) = \frac{\lambda_q}{6} \left[\hat{x} - \left(\frac{18}{\lambda_q^2}\right)^{1/3} \right]^2, \quad (34)$$

which recovers the result obtained by Pritchard *et al.* [16,18]. The steady-state current length \hat{x}_f can then be calculated from the result above, which yields $\hat{x}_f = (18/\lambda_q^2)^{1/3}$. If $\hat{x}_f < 1$, or equivalently

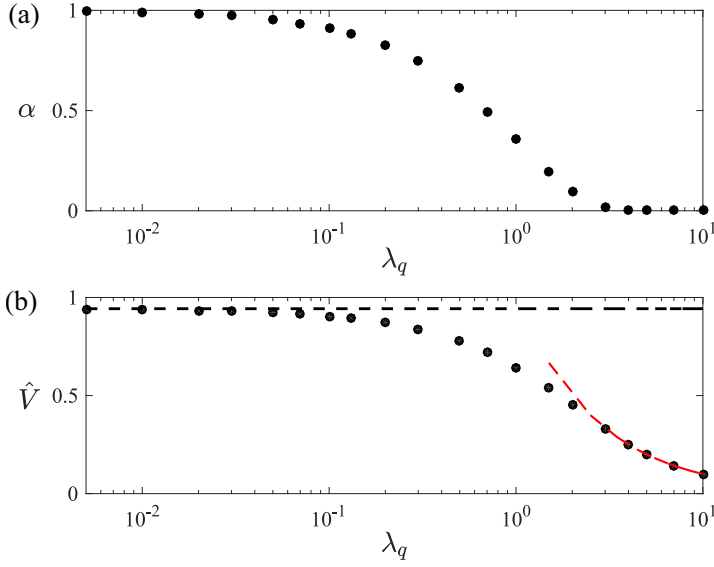


FIG. 9. Steady-state edge drainage fraction α and the steady-state volume \hat{V} for $\lambda_q = \{5 \times 10^{-3}, [1, 2, 3, 5, 7] \times 10^{-2}, [1, 1.3, 2, 3, 5, 7] \times 10^{-1}, 1, 1.5, 2, 3, 4, 5, 7, 10\}$. The results are obtained from solving Eq. (28) until the steady-state profiles are reached. (a) As $\lambda_q \rightarrow 0$, which represents the case of pure edge drainage, $\alpha \rightarrow 1$. For $\lambda_q > 5$, $\alpha = 0$ since the current tip has retracted from the edge and fluid only drains from the permeable base. (b) As $\lambda_q \rightarrow 0$, the current volume in the reservoir reaches its maximum value $2\sqrt{2}/3$ [as calculated using Eq. (35)], which is marked as the dashed line for a reference. On the other hand, $\hat{V} \rightarrow 0$ as $\lambda_q \rightarrow \infty$. When λ_q is large enough to prevent the gravity current from overshooting, the steady-state volume $\hat{V} \sim \lambda_q^{-1}$, as shown by the red dashed curve.

$\lambda_q > 3\sqrt{2}$, the gravity current only drains from the permeable substrate and the substrate length scale L can be treated as infinite, since the system loses information about the edge.

At the other limit, when $\lambda_q = 0$, fluid can only drain from the edge and $\hat{x}_f = 1$. In this case, Eq. (32) can be simplified and the solution is

$$\hat{h}_s(\hat{x}) = \sqrt{2(1 - \hat{x})}, \quad (35)$$

which recovers the result from the literature (see, e.g., [16,23,33]).

As a practical consideration, we are interested in the change of the drainage fraction $\alpha = \hat{q}_{\text{edge}}/\hat{q}$ with λ_q and also the amount of fluid that can be stored in the reservoir at the steady state. The results for these two quantities are provided in Fig. 9 based on the numerical calculations. Intuitively, one expects that $\alpha \rightarrow 1$ as $\lambda_q \rightarrow 0$, gradually decreases as λ_q increases, and stays zero above some critical value of λ_q . On the other hand, the volume of fluid that can be stored in the reservoir $\hat{V} \equiv \int_0^{\hat{x}_f} \hat{h}_s(\hat{x}) d\hat{x}$ will reach its maximum value $\hat{V} = 2\sqrt{2}/3$, computed using Eq. (35), as $\lambda_q \rightarrow 0$ and decreases as λ_q increases, which is consistent with the numerical results in Figs. 9(a) and 9(b). In fact, we can obtain the variation of \hat{V} at large λ_q . When the gravity current is not overshooting the edge $\hat{x}_f < 1$, Eq. (31) indicates that $\hat{V} = \lambda_q^{-1}$, which is plotted in Fig. 9(b) and shows good agreement with the numerical results.

B. Uniform drainage

In this section we are interested in a situation where there is a gravity current with constant loss at rate v_0 , while the vertical velocity in the propagating current is still much smaller than the horizontal velocity ($v_0 \ll u$). This configuration is proposed for some practical flow problems. For example,

a homogeneous and constant fluid loss should be considered when a gravity current experiences dissolution-driven convection to the ambient fluid, as verified by experiments [36]. This is equivalent to the case where a uniform and constant vertical draining rate v_0 through a permeable substrate is considered. Assuming that the vertical volume flux per unit width is a constant v_0 , using (1) and (2), the evolution equation for the profile shape $h(x, t)$ has the form

$$\frac{\partial h}{\partial t} = \frac{\Delta \rho g k}{\phi \mu} \frac{\partial}{\partial x} \left(h \frac{\partial h}{\partial x} \right) - \frac{v_0}{\phi}. \quad (36)$$

We next consider the solutions to this equation for the distinct cases of finite-volume release and constant flow rate injection.

1. Finite volume

When a finite volume of fluid is suddenly released, the governing equation (36) satisfies the initial and boundary conditions

$$h(x, 0) = \begin{cases} h_0, & 0 \leq x \leq L \\ 0, & x > L, \end{cases} \quad (37a)$$

$$\left. \frac{\partial h}{\partial x} \right|_{x=0} = 0, \quad h(L, t) = 0. \quad (37b)$$

The governing equation (36) and its initial and boundary conditions (37a) and (37b) can be nondimensionalized following the definition of dimensionless variables in Eq. (7) and we obtain

$$\frac{\partial \hat{h}}{\partial \hat{t}} = \frac{\partial}{\partial \hat{x}} \left(\hat{h} \frac{\partial \hat{h}}{\partial \hat{x}} \right) - \epsilon, \quad (38a)$$

$$\hat{h}(\hat{x}, 0) = \begin{cases} 1, & 0 \leq \hat{x} \leq 1 \\ 0, & \hat{x} > 1, \end{cases} \quad (38b)$$

$$\left. \frac{\partial \hat{h}}{\partial \hat{x}} \right|_{\hat{x}=0} = 0, \quad \hat{h}(1, \hat{t}) = 0, \quad (38c)$$

where ϵ is a dimensionless constant defined as

$$\epsilon \equiv \frac{v_0 \mu L^2}{\Delta \rho g k h_0^2} \ll 1. \quad (39)$$

We solved Eq. (38a) subject to (38b) and (38c) using a finite-difference scheme (Appendix) to obtain the profile shape evolutions shown in Fig. 10 for $\epsilon \ll 1$. Initially, the gravity current drains via both the permeable substrate and the edge. However, as the profile height continues to decrease, the front of the gravity current starts to retract, after which the gravity current only drains from the permeable substrate, until the initial volume is drained out at a finite time \hat{t}_{end} .

As the front starts to retract from the edge, the gravity current gradually loses information about the finite substrate length scale and the profile shapes shown in Fig. 10(a) inspire us to seek a self-similar solution. The time-dependent variations of profile height at the origin $\hat{h}(0, \hat{t})$ and the gravity current frontal location $\hat{x}_f(\hat{t})$ are shown in Figs. 10(b) and 10(c). We define $\tau_e \equiv \hat{t}_{\text{end}} - \hat{t}$. From numerical results, we observe that as $\tau_e \rightarrow 0$, $\hat{h}(0, \hat{t})$ and $\hat{x}_f(\hat{t})$ show a power-law dependence in time, where

$$\hat{h}(0, \hat{t}) = \epsilon \tau_e, \quad \hat{x}_f(\hat{t}) = A \tau_e^{1/2}, \quad (40)$$

with $A = 0.4$ being a fitting parameter.

Based on the form of Eq. (38a), a scaling analysis can be performed at $\tau_e \rightarrow 0$. According to (40), the diffusion term in Eq. (38a) scales as $\frac{\partial}{\partial \hat{x}} \left(\hat{h} \frac{\partial \hat{h}}{\partial \hat{x}} \right) = O(\tau_e)$, which becomes negligible as $\tau_e \rightarrow 0$.

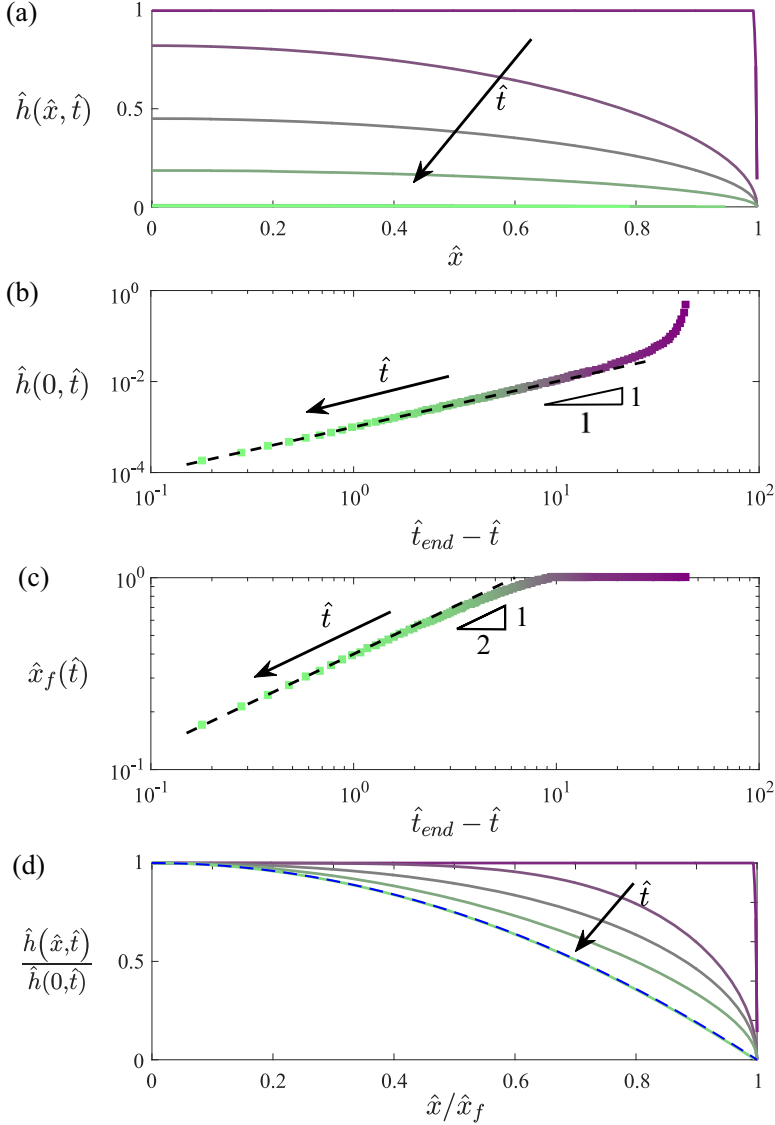


FIG. 10. (a) Numerical solutions to Eq. (38) showing the evolution of the current profile with time, with $\epsilon = 10^{-3}$, $\hat{t} = \{0, 0.3, 1.2, 4.0, 37, 40\}$. (b) Time evolution of current height at the origin $\hat{h}(0, \hat{t})$. As time progresses towards \hat{t}_{end} , $\hat{h}(0, \hat{t})$ is proportional to $\hat{t}_{\text{end}} - \hat{t}$. The black dashed line represents the theoretical prediction $\hat{h}(0, \hat{t}) = \epsilon(\hat{t}_{\text{end}} - \hat{t})$. (c) Time evolution of the current front location $\hat{x}_f(\hat{t})$. As time progresses towards \hat{t}_{end} , $\hat{x}_f(\hat{t})$ follows a power law $(\hat{t}_{\text{end}} - \hat{t})^{1/2}$. (d) Rescaling the numerical results to show the evolution of the stretched current profile \hat{x}/\hat{x}_f versus $\hat{h}/\hat{h}(0)$ with time, with $\epsilon = 10^{-3}$, $\hat{t} = \{0, 0.03, 0.1, 30, 44\}$. The self-similar solution (42) is given as the blue dashed curve for a comparison. At $\hat{t} = 44$, for example, the rescaled profile already overlaps with the self-similar solution.

Thus the leading-order behavior becomes $\hat{h}/\tau_e = O(\epsilon)$, which suggests that the profile height has the form

$$\hat{h}(\hat{x}, \hat{t}) = \epsilon[\tau_e - \tau_0(\hat{x})], \quad (41)$$

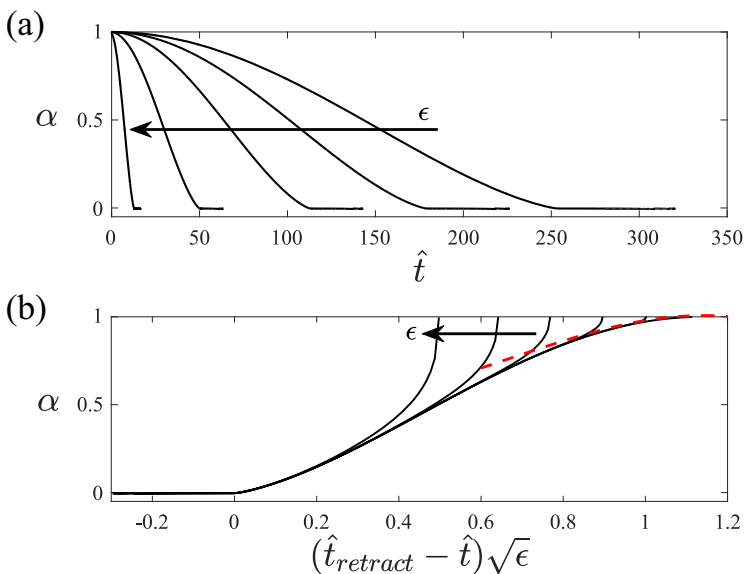


FIG. 11. Drainage fraction α variation with time. (a) Numerical results of the drainage fraction $\alpha = \hat{q}_{\text{edge}}/\hat{q}$ as a function of time \hat{t} , with $\epsilon = \{2 \times 10^{-5}, 4 \times 10^{-5}, 10^{-4}, 5 \times 10^{-4}, 7 \times 10^{-3}\}$. (b) After rescaling time as $(\hat{t}_{\text{retract}} - \hat{t})\sqrt{\epsilon}$, the results in (a) collapse to a universal curve, with $\epsilon = \{10^{-5}, 3 \times 10^{-2}, 10^{-1}, 2.5 \times 10^{-1}, 5 \times 10^{-1}, 1\}$. The theoretically predicted early-time behavior (44) is shown as the red dashed curve, which shows good agreement with the universal curve.

where τ_0 is a function of \hat{x} , and $\tau_0(\hat{x}) = (\hat{x}/A)^2$ can be further determined based on the frontal location in Eq. (40). Thus, Eq. (41) can be rewritten as

$$\frac{\hat{h}(\hat{x}, \hat{t})}{\hat{h}(0, \hat{t})} = 1 - \left(\frac{\hat{x}}{\hat{x}_f(\hat{t})} \right)^2. \quad (42)$$

The profile evolution shown in Fig. 10(a) is rescaled and shown in Fig. 10(d), along with the self-similar profile (42), which exhibit good agreement. Notice that the retraction of a gravity current draining from a substrate was also observed by Pritchard *et al.* [18] and in this particular regime the same universal shape (42) is obtained. Nevertheless, the values for $\hat{h}(0, \hat{t})$ and $\hat{x}_f(\hat{t})$ in this problem are obtained numerically from solving Eq. (38) and cannot be predicted directly from the solutions of Pritchard *et al.* [18].

The drainage fraction through the edge α , which is defined as $\alpha = \hat{q}_{\text{edge}}/\hat{q}$, can also be calculated numerically. Figure 11(a) displays the time variation of α for different values of ϵ . We define \hat{t}_{retract} as the time when the gravity current starts to retract. As the finite volume of fluid is released, initially the fluid mainly drains from the edge ($\alpha \approx 1$). The value of α decreases to zero at a finite time \hat{t}_{retract} and remains $\alpha = 0$ until the fluid drains out at \hat{t}_{end} . Since the variation of α only occurs when $0 < \hat{t} < \hat{t}_{\text{retract}}$, in order to eliminate the ϵ dependence, the nondimensional time is rescaled and the results in Fig. 11(a) collapse to a universal curve shown in Fig. 11(b).

We note that in the limit $\epsilon \rightarrow 0$, edge drainage dominates at the early times ($\hat{t} \ll \hat{t}_{\text{retract}}$) and the profile shape can be approximated by that in the case of pure edge drainage [20]. Thus, $\hat{h}(\hat{x}, \hat{t})$ satisfies $\hat{h}(\hat{x}, \hat{t}) = \hat{t}^{-1} f(\hat{x})$, where $f(\hat{x})$ is identical to the self-similar solution (15). Therefore, the edge drainage flow rate can be obtained:

$$\hat{q}_{\text{edge}} \equiv -\hat{h} \frac{\partial \hat{h}}{\partial \hat{x}} \Big|_{\hat{x}=1} = -(ff')|_{\hat{x}=1} \hat{t}^{-2}. \quad (43)$$

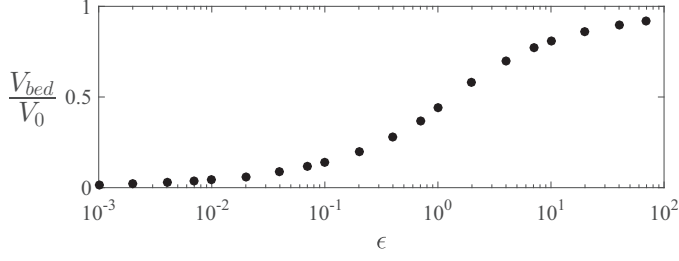


FIG. 12. Numerical results showing the final volume fraction of fluid drained from the base for different dimensionless drainage parameter ϵ , defined in Eq. (39). The current has a rectangular initial condition (38b) and $\epsilon = \{[1, 2, 4, 7] \times 10^{-3}, [1, 2, 4, 7] \times 10^{-2}, 0.1, 0.2, 0.4, 0.7, 1, 2, 4, 7, 10, 20, 40, 70\}$.

We define $z \equiv -(ff')_{\hat{x}=1}$ and according to the numerical calculation, $z \approx 0.693$. Hence, the drainage fraction α can be derived as

$$\alpha(\hat{t}) = \frac{z\hat{t}^{-2}/\epsilon}{z\hat{t}^{-2}/\epsilon + 1}. \quad (44)$$

We picked a small value of $\epsilon = 10^{-5}$ and plotted (44) in Fig. 11(b) as the red dashed curve. This result shows good agreement with the universal curve at the early times. In the limit $\epsilon \rightarrow 0$, $\hat{t}_{\text{retract}} \rightarrow \infty$ and the curve stays at the asymptotic value $\alpha = 1$, which is consistent with the case of pure edge drainage.

When a fixed amount of fluid is suddenly released, one of the practical concerns is the fraction of fluid that the gravity current loses through draining from the permeable substrate. In dimensional terms, we define V_{bed} as the final volume of fluid that drains through the permeable substrate, which depends on ϵ as defined in Eq. (39) and is reported relative to the initial volume $V_0 = h_0 L$. Intuitively, the volume fraction $V_{\text{bed}}/V_0 \rightarrow 1$ as $\epsilon \rightarrow \infty$, while $V_{\text{bed}}/V_0 \rightarrow 0$ as $\epsilon \rightarrow 0$. Numerical results for V_{bed}/V_0 as a function of a large range of ϵ are reported in Fig. 12 in order to show the asymptotic trend; the results are consistent with this argument. Notice that in natural situations, the condition $\epsilon \ll 1$ usually applies due to the small vertical drainage rate v_0 .

2. Constant injection rate

If there is a continuous supply of fluid with a constant flow rate q at the origin $x = 0$, the fluid flow will eventually evolve to a steady state. Now the governing equation and initial and boundary conditions are

$$\frac{\partial h}{\partial t} = \frac{\Delta \rho g k}{\phi \mu} \frac{\partial}{\partial x} \left(h \frac{\partial h}{\partial x} \right) - \frac{v_0}{\phi}, \quad (45a)$$

$$h(x, 0) = 0, \quad (45b)$$

$$h \frac{\partial h}{\partial x} \Big|_{x=0} = -\frac{q \phi \mu}{\Delta \rho g k}, \quad h(L, t) = 0. \quad (45c)$$

After nondimensionalization, following Eq. (27), we arrive at

$$\frac{\partial \hat{h}}{\partial \hat{t}} = \frac{\partial}{\partial \hat{x}} \left(\hat{h} \frac{\partial \hat{h}}{\partial \hat{x}} \right) - \epsilon_q, \quad (46a)$$

$$\hat{h}(\hat{x}, 0) = 0, \quad (46b)$$

$$\hat{h} \frac{\partial \hat{h}}{\partial \hat{x}} \Big|_{\hat{x}=0} = -1, \quad \hat{h}|_{\hat{x}=1} = 0, \quad (46c)$$

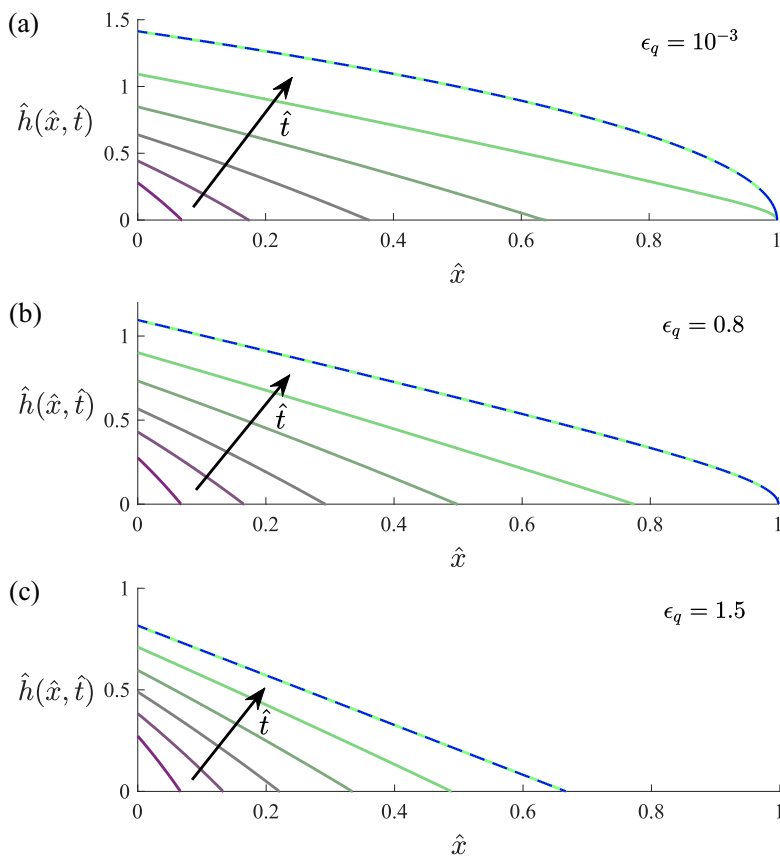


FIG. 13. Evolution of a current with a constant injection rate $\hat{h} \frac{\partial \hat{h}}{\partial \hat{x}} = -1$ at the origin. Fluid drains from both the base and the edge, with $\epsilon_q = \{10^{-3}, 0.8, 1.5\}$. As time progresses, the current gradually evolves to its steady-state profile, where color is used to display the time evolution. The corresponding steady-state solution (52) or (53) is shown as a blue dashed curve in each case as a comparison: (a) $\epsilon_q = 10^{-3}$, the gravity current overshoots the edge, for times $\hat{t} = \{0.01, 0.04, 0.12, 0.28, 0.6, 10\}$; (b) $\epsilon_q = 0.8$, the gravity current overshoots the edge, for times $\hat{t} = \{0.01, 0.04, 0.1, 0.25, 0.6, 10\}$; and (c) $\epsilon_q = 1.5$, the gravity current only drains from the permeable base, for times $\hat{t} = \{0.01, 0.03, 0.07, 0.15, 0.35, 10\}$.

where ϵ_q is defined as

$$\epsilon_q \equiv \frac{v_0 L}{\phi q}. \quad (47)$$

Equation (46a) can now be solved numerically subject to the initial and boundary conditions (46b) and (46c) and results in different current profile evolutions for different values of ϵ_q . Figure 13 presents three typical shape evolutions at $\epsilon_q = 10^{-3}$, 0.8, and 1.5. As time progresses, the current profiles are marked with the gradually changing colors from purple to green.

We are interested in investigating the effect of ϵ_q on the steady-state current profiles. Since the governing equation is then invariant with time, Eq. (46) becomes

$$\frac{d^2 \hat{h}_s^2}{d\hat{x}^2} = 2\epsilon_q, \quad (48a)$$

$$\hat{h}_s \left. \frac{d\hat{h}_s}{d\hat{x}} \right|_{\hat{x}=0} = -1, \quad \hat{h}_s(\hat{x}_f) = 0, \quad (48b)$$

where $\hat{h}_s(\hat{x})$ represents the profile shape at the steady state. Note that the boundary condition is refined as $\hat{h}_s(\hat{x}_f) = 0$ to remind us that if the gravity current is not overshooting from the edge ($\hat{x}_f \neq 1$), extra information about the frontal location \hat{x}_f is required to close the problem. This information can be obtained based on the fact that the total drainage rate from the permeable substrate is now balanced by the fluid injection rate at the origin

$$\epsilon_q \hat{x}_f = 1, \quad (49)$$

which leads to $\hat{x}_f = 1/\epsilon_q$ for $\epsilon_q \geq 1$. When $\epsilon_q < 1$, the gravity current overshoots the edge. In such case, $\hat{x}_f = 1$ and the boundary condition $\hat{h}_s(1) = 0$ is imposed.

There exists an analytical solution to Eq. (48a), subject to boundary conditions (48b) and (49):

$$\hat{h}_s(\hat{x}) = \sqrt{\epsilon_q \hat{x}^2 - 2\hat{x} + c}, \quad (50)$$

where c is a non-negative integration constant that is related to the steady-state profile height at the origin

$$c = [\hat{h}_s(0)]^2. \quad (51)$$

We note that Eq. (50) has been shown previously, for example, in Ref. [33]. When the gravity current overshoots the edge, the integration constant $c = 2 - \epsilon_q$ can be determined by applying the boundary condition $\hat{h}_s(1) = 0$ and the solution becomes

$$\hat{h}_s(\hat{x}) = \sqrt{\epsilon_q \hat{x}^2 - 2\hat{x} + 2 - \epsilon_q}. \quad (52)$$

Equation (52) requires $\epsilon_q < 1$ to ensure that the value of current height $\hat{h}_s(\hat{x})$ remains real in the entire domain of $\hat{x} \in [0, 1]$. In particular, at the limit of $\epsilon_q = 0$, the steady-state solution (35) is again recovered [16,23,33]. In such a case, fluid only drains from the edge.

If $\epsilon_q > 1$, Eq. (52) fails to have real values for the entire region of $\hat{x} \in [0, 1]$. Physically, this means that $\hat{x}_f < 1$ and fluid only drains from the permeable base. Therefore, by applying the boundary condition $\hat{h}_s(\hat{x}_f) = 0$, the integration constant c in Eq. (50) can be determined as $c = 1/\epsilon_q$ and we recover the solution obtained by Pritchard *et al.* [18]:

$$\hat{h}_s(\hat{x}) = \frac{1}{\sqrt{\epsilon_q}}(1 - \epsilon_q \hat{x}). \quad (53)$$

Analytic results (52) and (53) with different values of ϵ_q are displayed with the numerical solutions to Eq. (46) at different times in Fig. 13 in order to highlight the profile shape evolution towards the steady state; the results exhibit good agreement. Furthermore, the final shapes are displayed as a function of ϵ_q in Fig. 14, provided by the analytical solutions (52) and (53) for $\hat{h}_s(\hat{x})$. The rescaled steady-state profiles of Fig. 14(a) are also shown in Fig. 14(b) and the rescaled profiles vary from convex curves to straight lines as ϵ_q increases.

We are also interested in determining the ratio of fluid draining flux from the edge versus the total drainage flux at the steady state $\alpha \equiv q_{\text{edge}}/q$. We already know that the ratio at $\epsilon_q > 1$ approaches zero, since fluid only drains through the permeable base. At $\epsilon_q < 1$, knowing that $\hat{q}_{\text{bed}} = \epsilon_q \hat{x}_f = \epsilon_q$, the drainage rate fraction can then be determined as $\alpha = 1 - \epsilon_q$ when the current is overshooting from the edge. Thus, α can be summarized as

$$\alpha = \frac{\hat{q}_{\text{edge}}}{\hat{q}} = \begin{cases} 1 - \epsilon_q, & 0 \leq \epsilon_q \leq 1 \\ 0, & \epsilon_q > 1. \end{cases} \quad (54)$$

III. IMPLICATIONS FOR CO₂ SEQUESTRATION PROJECTS

The work in this paper is partly inspired by the practical concerns related to the leakage of the supercritical CO₂ from geological sequestration projects [37–43], in which the determination of

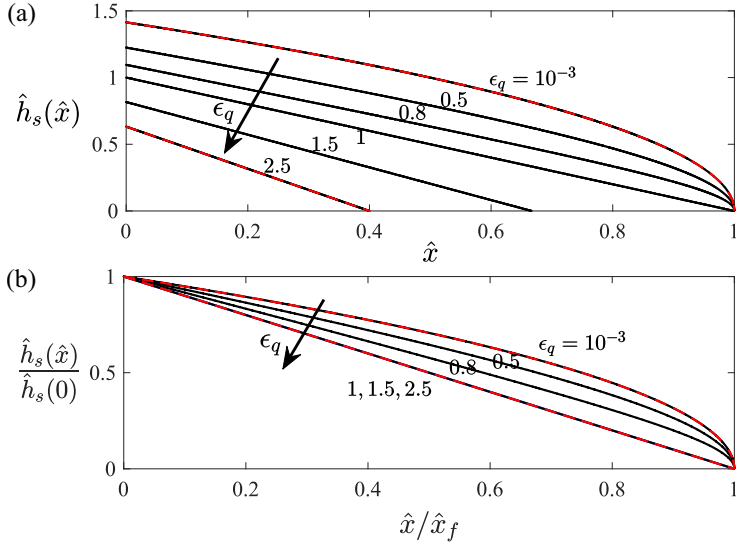


FIG. 14. Under constant flow rate fluid injection, steady-state profile variation with different values of ϵ_q . (a) Steady-state profile shapes variation with $\epsilon_q = \{10^{-3}, 0.5, 0.8, 1, 1.5, 2.5\}$. Analytical solutions (52) and (53) with different values of ϵ_q are displayed and show good agreement with the profile shapes at the limits $\epsilon_q > 1$ (i.e., $\hat{x}_f < 1$) (from Refs. [16,18]) and $\epsilon_q \rightarrow 0$ (from Refs. [16,23,33]), which are shown as red dashed curves. (b) Rescaled steady-state profiles in (a). After normalization, the curves corresponding to $\epsilon_q = \{1, 1.5, 2.5\}$ collapse with one another and agree with the rescaled solution (52) [16,18]. As the value of λ_q increases, the steady-state profile shape changes from a straight line to a concave shape.

the current profile shapes is crucial, since it is closely related to the amount of CO_2 that can be stored underground and the prediction of the storage time scale. Permeable substrate drainage and edge drainage are among the most commonly discussed leakage mechanisms. It is known that the gravity current profiles predicted from the two different leakage mechanisms are distinguished from one another [16,18,23]. Therefore, in this paper we have studied the viscous gravity current profile and the competition between the two drainage mechanisms using both theoretical analyses and numerical simulations. Note that in the theoretical and numerical analyses above, the gravity current fluid is assumed to be denser than the ambient fluid. However, in CO_2 sequestration projects, CO_2 is less dense than the surrounding brine. Thus, buoyancy is pointing upward rather than downward, as assumed in the paper thus far, but the theoretical results still apply on reversal of the vertical coordinate.

As one of the possible ways to slow down the accumulation of CO_2 in the atmosphere, the demonstration project of CO_2 storage in the Utsira sand reservoir at Sleipner in the North Sea was started in 1996 [17,19,22,44–47]. Thus, there is an industrial interest in the case of a buoyancy-driven current subject to constant fluid injection. Upon injection, CO_2 is captured beneath several thin layers of mudstone (caprock). Due to the limited length of the thin mudstone layers and low yet not negligible permeability of the caprocks, permeable substrate drainage and edge drainage become important factors that may lead to a possible long-term storage problem beneath the caprock. It is therefore crucial to determine the storage capability of each mudstone layer and the steady-state current profile.

According to the analysis in Sec. II A 2, we know that the nondimensional drainage parameter λ_q needs to be greater than $3\sqrt{2} \approx 4.2$ in order to prohibit the edge drainage and it is required for $\lambda_q \rightarrow 0$ to eliminate the effects of the substrate drainage. In order to maximize the storage capability of each mudstone, the calculation here is therefore based on $\hat{x}_f = 1$. For the limit of dominant substrate drainage, the current profile satisfies Eq. (34), with the critical parameter $\lambda_{qc} = 3\sqrt{2}$, and

TABLE I. Physical parameters in practical CO₂ geological sequestration projects.

	CO ₂ density ρ_c (kg/m ³)	Brine density ρ_w (kg/m ³)	CO ₂ viscosity μ (Pa s)	Reservoir porosity ϕ	Reservoir permeability k (m ²)	Base permeability k_b (m ²)	Injection rate/width q (Mt/year m)	Permeable base thickness b (m)	Permeable base length L (m)
Range	(2.7– 7.3) × 10 ²	(9.5 × 10 ²)– (1.2 × 10 ³)	(3.0– 5.0) × 10 ⁻⁵	0.20–0.60 0.20–0.60	(2.3– 6.1) × 10 ⁻¹²	(5.8 × 10 ⁻¹⁹)– (1.1 × 10 ⁻¹⁶)	0.50–3.5	1.0–5.0	(2.3 × 10 ³)– (2.7 × 10 ⁵)
Benchmark values	5.0 × 10 ²	1.1 × 10 ³	4.0 × 10 ⁻⁵	0.40	4.2 × 10 ⁻¹²	5.5 × 10 ⁻¹⁷	2.0	3.0	1.4 × 10 ⁵
Reference	[5,45]	[5,45]	[5,45]	[45,48]	[45]	[48]	[5,45]	[45]	[49]

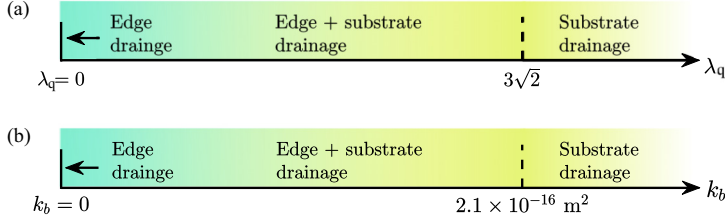


FIG. 15. Drainage regime based on the drainage mechanism. (a) Drainage regime based on the drainage parameter λ_q . When $\lambda_q \rightarrow 0$, current drainage can be considered as edge drainage dominant. When $\lambda_q \gg 3\sqrt{2}$, substrate drainage is dominant. While $0 < \lambda_q \ll 3\sqrt{2}$, one should consider the coupled drainage effect due to both a fixed edge and a permeable substrate and the results provided in Sec. II A 2 apply. (b) Drainage regime example based on substrate permeability k_b . Drainage regimes can be defined similarly based on the substrate permeability, given that the mean values of the other properties are used.

the nondimensional volume of the steady-state current is $\hat{V} = \sqrt{2}/6 \approx 0.24$. Using the definition in Eq. (29), we can compute the critical value of substrate permeability k_b based on the critical $\lambda_{q_c} = 3\sqrt{2}$ and the benchmark values listed in Table I for $\Delta\rho$, g , k , L , ϕ , μ , q , and b . This leads to $k_b = 2.1 \times 10^{-16} \text{ m}^2$, as shown by the dashed line in Fig. 15(b), and the steady-state current volume per unit width becomes $V = 2.5 \times 10^9 \text{ m}^2$.

If the edge drainage dominant limit is considered instead, $\lambda_q = 0$, which also corresponds to an impermeable substrate with $k_b = 0$. The current profile satisfies Eq. (35) and the nondimensional volume of the steady-state current now becomes $\hat{V} = 2\sqrt{2}/3 \approx 0.94$, which corresponds to a dimensional volume per unit width $V = 1.0 \times 10^{10} \text{ m}^2$.

Now we take into account the reported parameters involved in a CO₂ sequestration project, which is tabulated in Table I based on studies about permeability of natural mudstone. According to (29), the value of λ_q can vary from 4.1×10^{-6} to 99. Yet if the benchmark value of each parameter is used, the corresponding $\lambda_q = 1.1$, which falls into the coupled drainage regime. In this case, the nondimensional volume is $\hat{V} = 0.62$, which corresponds to a dimensional volume per unit width $V = 6.6 \times 10^9 \text{ m}^2$.

As shown in the calculation above, the estimated storage capacity differs significantly with and without the consideration of the coupled drainage mechanisms. As discussed in Sec. II A 2, the drainage coefficient λ_q is the parameter that indicates the drainage regime and among all the properties considered, the permeability of the mudstone is one of the most important. Thus, using the benchmark value of the other properties, one can also determine the drainage regime depending on the value of the mudstone permeability k_b , as sketched in Fig. 15.

It is also worth pointing out that once the constant fluid injection is stopped, the current spreading problem then falls into the finite-volume drainage regime. It is of particular interest to understand the time scale at which the majority of the fluid is drained out and the amount of fluid that will drain from the edge. We assume a rectangular initial condition so as to provide a relative time scale for the sake of comparison. The following results are obtained from numerically solving Eq. (8a) with different values of λ , as defined in Eq. (9). Using the benchmark values of the properties (Table I), if pure edge drainage is considered ($k_b = 0$), it requires $\hat{t} = 61$ in order to drain out 90% of the fluid. This dimensional time corresponds to $t = 2.1 \times 10^4$ years. If both substrate and edge drainage are considered instead, taking $\lambda = 1.1$, the dimensionless time is $\hat{t} = 1.9$. Therefore, $t \approx 640$ years are required to drain 90% of the fluid, 76% of which is drained through the substrate. Note that the gravity current drainage rate may deviate from the exponential relationship shown in Eq. (8a) due to the accumulated defects in caprock or dissolution of CO₂ in brine after long-term storage. Nevertheless, the theoretical results from this study point out the relative significance of substrate drainage over edge drainage for the long-term CO₂ storage.

TABLE II. Summary of equations and solutions of buoyancy-driven drainage.

Model	Finite volume	Constant flux
PDE or ODE	$\left(\frac{\phi\mu}{\Delta\rho gk}\right)\frac{\partial h}{\partial t} = \frac{\partial}{\partial x}\left(h\frac{\partial h}{\partial x}\right) - \frac{k_b h}{kb}$	$\frac{\partial}{\partial x}\left(h\frac{\partial h}{\partial x}\right) = \frac{k_b h}{kb}$
initial condition	$h(x,0) = \begin{cases} h_0, & 0 \leq x \leq L \\ 0, & x > L \end{cases}$	$h(x,0) = 0 \quad (0 \leq x \leq L)$
boundary conditions	Early time: $h(0,t) = h_0$ $h(L,t) = 0$	Late time: $\frac{\partial h}{\partial x}(0,t) = 0$ $h(L,t) = 0$
solution	$H = \psi(\eta), \quad \eta = \frac{\hat{x}-1}{\sqrt{2\tau}}$	$H = \frac{f(\hat{x})}{\tau}$
simplified ODE	$(\psi\psi')' + \eta\psi' = 0$ $\psi(-\infty) = 1$ $\psi(0) = 0$	$(ff')' + f = 0$ $f'(0) = 0$ $f(1) = 0$
drainage fraction α	$\alpha = \exp(-\lambda\hat{t}) \quad (\lambda \ll 1, \text{ late time})$	$\frac{d\hat{h}_s^2}{d\hat{x}} = -\sqrt{\frac{8}{3}}\lambda_q\hat{h}_s^3 + c$ $\frac{d^2\hat{h}_s^2}{d\hat{x}^2} = 2\lambda_q\hat{h}_s$ $\hat{h}_s\left.\frac{\partial\hat{h}_s}{\partial\hat{x}}\right _{\hat{x}=0} = -1$ $\hat{h}_s(\hat{x}_f) = 0$ Fig. 9(a)
comments	$\lambda = \frac{k_b L^2}{kbh_0^2}, \quad H = \hat{h} \exp(\lambda\hat{t}), \quad \tau = \frac{1-\exp(-\lambda\hat{t})}{\lambda}$	$\lambda_q = \frac{k_b L}{kb} \left(\frac{\Delta\rho gkL}{q\phi\mu}\right)^{1/2}$

IV. SUMMARY AND CONCLUSIONS

In this paper we studied the dynamics of a gravity current in a homogeneous porous medium under the coupled effects of drainage from both a permeable substrate and a fixed edge. Furthermore, the substrate drainage is categorized as buoyancy-driven drainage or uniform drainage. In each category, both the case of a sudden release of a finite volume and the case of constant fluid injection are discussed. Using theoretical analyses and numerical simulations, we investigated the time evolution of current profiles and drainage rates through each of the mechanisms. For the cases of a finite-volume release, we obtained self-similar solutions and the fluid drainage flow rate fraction α through the edge. Specifically, for the buoyancy-driven drainage, we found that the drainage fraction varies as $\alpha = \exp(-\lambda_q\hat{t})$; for the uniform drainage case, we found that α varies with time following a universal curve [Fig. 11(a)].

For the cases of a continuous flow rate, we have presented steady-state current profiles, as well as the fluid loss through each drainage mechanism. In particular, for gravity-driven drainage, a simplified ODE (32) and its boundary conditions were obtained to describe the variation of the steady-state

TABLE III. Summary of equations and solutions for uniform flow drainage.

Model	Finite volume	Constant flux
PDE or ODE	$\frac{\partial h}{\partial t} = \frac{\Delta\rho gk}{\phi\mu} \frac{\partial}{\partial x}\left(h\frac{\partial h}{\partial x}\right) - \frac{v_0}{\phi}$	$\frac{\Delta\rho gk}{\phi\mu} \frac{\partial}{\partial x}\left(h\frac{\partial h}{\partial x}\right) = \frac{v_0}{\phi}$
initial condition	$h(x,0) = \begin{cases} h_0, & 0 \leq x \leq L \\ 0, & x > L \end{cases}$	$h(x,0) = 0 \quad (0 \leq x \leq L)$
boundary conditions	$\frac{\partial h}{\partial x}(0,t) = 0$ $h(L,t) = 0$	$h\frac{\partial h}{\partial x}(0,t) = -\frac{q\phi\mu}{\Delta\rho gk}$ $h(L,t) = 0$
solution	$\frac{\hat{h}(\hat{x},\hat{t})}{\hat{h}(0,\hat{t})} = 1 - \left(\frac{\hat{x}}{\hat{x}_f(\hat{t})}\right)^2$	$\hat{h}_s(\hat{x}) = \begin{cases} \sqrt{\frac{\epsilon_q\hat{x}^2 - 2\hat{x} + 2 - \epsilon_q}{\sqrt{\epsilon_q}}(1 - \epsilon_q\hat{x})}, & 0 \leq \epsilon_q \leq 1 \\ \frac{d^2\hat{h}_s^2}{d\hat{x}^2} = 2\epsilon_q, & \epsilon_q > 1 \end{cases}$ $\hat{h}_s\left.\frac{\partial\hat{h}_s}{\partial\hat{x}}\right _{\hat{x}=0} = -1$ $\hat{h}_s(\hat{x}_f) = 0$
simplified ODE		$\alpha = \begin{cases} 1 - \epsilon_q, & 0 \leq \epsilon_q \leq 1 \\ 0, & \epsilon_q > 1 \end{cases}$
drainage fraction α	Figs. 11(a) and 11(b)	
comments	$\epsilon = \frac{v_0\mu L^2}{\Delta\rho gk h_0^2}$	$\epsilon_q = \frac{v_0 L}{\phi q}$

profile along with different values of the drainage parameter λ_q ; the results for the drainage fraction α and the amount of fluid remaining in the reservoir are shown in Fig. 9. For the uniform flow drainage, an analytical solution (50) was obtained, depending on the value of ϵ_q . In addition, the drainage fraction α was obtained analytically and $\alpha = 1 - \epsilon_q$ if $\epsilon_q < 1$ and $\alpha = 0$ otherwise. A summary of the equations and solutions included in this paper is listed in Tables II and III.

The investigation of the coupled drainage effects on a gravity current can provide useful insights into the CO₂ sequestration projects and other subsurface flows. As mentioned in Sec. III, understanding the coupled effects can provide a better approximation for the fluid storage capability under caprocks, as well as the time required for possible CO₂ leakage. Although the permeability of the caprock is typically very small, the relevant time scales are large and therefore the drainage effect through the caprock may be significant, which can influence CO₂ geological storage problems. The results in this paper provide a model that may help better design CO₂ sequestration procedures and make better use of the natural reservoirs to ensure the success of long-term CO₂ storage projects.

ACKNOWLEDGMENTS

This work started as a final project at Princeton University in a graduate course offered by Z.Z. and H.A.S. Z.Z. hereby thanks the Princeton Carbon Mitigation Initiative (CMI) for the partial support from a CMI Young Investigator Award. Y.E.Y. and H.A.S. are grateful for the partial support from the National Science Foundation Training Grant in the Mathematical Methods for Water Problems (Grant No. AWD1004562, PI=P. Constantin). We also thank the two anonymous referees for helpful comments.

APPENDIX: NUMERICAL SIMULATION

A cell-centered, forward-time, finite-difference scheme is chosen to solve the partial differential equations. For each drainage parameter chosen, a convergence test is performed in order to ensure that the maximum error in current height $\Delta \hat{h}(\hat{x}, \hat{t}) / \hat{h}(\hat{x}, \hat{t})$ is within 0.5% of $\hat{h}(\hat{x}, \hat{t})$ when the number of grid points is doubled or the numerical simulation time is doubled. A stability analysis for the numerical simulations was not performed, but the time step Δt was chosen such that no instability was observed within the time interval of interest. The equations used as an approximation of the terms in the nonlinear PDE (8a) are

$$\hat{h}_i^{n+1} = \left(\frac{J_{i+1/2}^n - J_{i-1/2}^n}{\Delta x} - \lambda \right) \Delta t + \hat{h}_i^n, \quad (\text{A1})$$

$$J_{i+1/2}^n = \left(\frac{\hat{h}_{i+1}^n + \hat{h}_i^n}{2} \right) \left(\frac{\hat{h}_{i+1}^n - \hat{h}_i^n}{\Delta x} \right), \quad (\text{A2})$$

where \hat{h}_i^n stands for the current height at the i th grid at time $n\Delta t$ and $J_{i+1/2}^n$ represents the flux into the i th grid at time $n\Delta t$.

In the cases where the front of the current is not pinned at the edge for all time, grid refinement is carried out. Take the retracting current in Sec. II B 1 as an example, the grids are originally defined in a spatial region $\hat{x} \in [0, 1]$ as the finite volume of fluid is released. As the current length shrinks to half of the domain size, the space is redefined in domain $\hat{x} \in [0, 1/2]$ with the same number of grid points to ensure accuracy. This refinement is carried out five times before the current is completely drained. A convergence test is performed for each refinement.

-
- [1] H. E. Huppert and A. W. Woods, Gravity-driven flows in porous layers, *J. Fluid Mech.* **292**, 55 (1995).
 [2] J. M. Nordbotten and M. A. Celia, Similarity solutions for fluid injection into confined aquifers, *J. Fluid Mech.* **561**, 307 (2006).

- [3] M. A. Hesse, H. A. Tchelepi, B. J. Cantwel, and F. M. Orr, Gravity currents in horizontal porous layers: Transition from early to late self-similarity, *J. Fluid Mech.* **577**, 363 (2007).
- [4] C. W. MacMinn, M. L. Szulczewski, and R. Juanes, CO₂ migration in saline aquifers. Part 1. Capillary trapping under slope and groundwater flow, *J. Fluid Mech.* **662**, 329 (2010).
- [5] H. E. Huppert and J. A. Neufeld, The fluid mechanics of carbon dioxide sequestration, *Annu. Rev. Fluid Mech.* **46**, 255 (2014).
- [6] S. S. Pegler, H. E. Huppert, and J. A. Neufeld, Fluid injection into a confined porous layer, *J. Fluid Mech.* **745**, 592 (2014).
- [7] Z. Zheng, B. Guo, I. C. Christov, M. A. Celia, and H. A. Stone, Flow regimes for fluid injection into a confined porous medium, *J. Fluid Mech.* **767**, 881 (2015).
- [8] B. Guo, Z. Zheng, M. A. Celia, and H. A. Stone, Axisymmetric flows from fluid injection into a confined porous medium, *Phys. Fluids* **28**, 022107 (2016).
- [9] B. Guo, Z. Zheng, K. W. Bandilla, M. A. Celia, and H. A. Stone, Flow regime analysis for geologic CO₂ sequestration and other subsurface fluid injections, *Int. J. Greenhouse Gas Con.* **53**, 284 (2016).
- [10] R. J. Glass and M. J. Nicholl, Physics of gravity fingering of immiscible fluids within porous media: An overview of current understanding and selected complicating factors, *Geoderma* **70**, 133 (1996).
- [11] A. W. Woods and R. Mason, The dynamics of two-layer gravity-driven flows in permeable rock, *J. Fluid Mech.* **421**, 83 (2000).
- [12] S. M. Taghavi, T. Seon, D. M. Martinez, and I. A. Frigaard, Buoyancy-dominated displacement flows in near-horizontal channels: The viscous limit, *J. Fluid Mech.* **639**, 1 (2009).
- [13] Z. Zheng, I. C. Christov, and H. A. Stone, Influence of heterogeneity on second-kind self-similar solutions for viscous gravity currents, *J. Fluid Mech.* **747**, 218 (2014).
- [14] Z. Zheng, L. Rongy, and H. A. Stone, Viscous fluid injection into a confined channel, *Phys. Fluids* **27**, 062105 (2015).
- [15] P. Dudfield and A. W. Woods, On the periodic injection of fluid into, and its extraction from, a porous medium for seasonal heat storage, *J. Fluid Mech.* **707**, 467 (2012).
- [16] D. Pritchard, Gravity currents over fractured substrates in a porous medium, *J. Fluid Mech.* **584**, 415 (2007).
- [17] M. A. Hesse and A. W. Woods, Buoyant dispersal of CO₂ during geological storage, *Geophys. Res. Lett.* **37** (2010).
- [18] D. Pritchard, A. W. Woods, and A. J. Hogg, On the slow draining of a gravity current moving through a layered permeable medium, *J. Fluid Mech.* **444**, 23 (2001).
- [19] J. A. Neufeld and H. E. Huppert, Modelling carbon dioxide sequestration in layered strata, *J. Fluid Mech.* **625**, 353 (2009).
- [20] Z. Zheng, B. Soh, H. E. Huppert, and H. A. Stone, Fluid drainage from the edge of a porous reservoir, *J. Fluid Mech.* **718**, 558 (2013).
- [21] S. E. King and A. W. Woods, Dipole solutions for viscous gravity currents: Theory and experiments, *J. Fluid Mech.* **483**, 91 (2003).
- [22] J. A. Neufeld, D. Vella, and H. E. Huppert, The effect of a fissure on storage in a porous medium, *J. Fluid Mech.* **639**, 239 (2009).
- [23] M. J. Golding, J. A. Neufeld, M. A. Hesse, and H. E. Huppert, Two-phase gravity currents in porous media, *J. Fluid Mech.* **678**, 248 (2011).
- [24] S. S. Pegler, E. L. Bain, H. E. Huppert, and J. A. Neufeld, Fluid invasion of an unsaturated leaky porous layer, *J. Fluid Mech.* **777**, 97 (2015).
- [25] J. A. Neufeld, D. Vella, H. E. Huppert, and J. R. Lister, Leakage from gravity currents in a porous medium. Part 1. A localized sink, *J. Fluid Mech.* **666**, 391 (2011).
- [26] D. Vella, J. A. Neufeld, H. E. Huppert, and J. R. Lister, Leakage from gravity currents in a porous medium. Part 2. A line sink, *J. Fluid Mech.* **666**, 414 (2011).
- [27] D. Pritchard and A. J. Hogg, Draining viscous gravity currents in a vertical fracture, *J. Fluid Mech.* **459**, 207 (2002).
- [28] J. M. Acton, H. E. Huppert, and M. G. Worster, Two-dimensional viscous gravity currents flowing over a deep porous medium, *J. Fluid Mech.* **440**, 359 (2001).

- [29] M. J. Spannuth, J. A. Neufeld, J. S. Wettlaufer, and M. G. Worster, Axisymmetric viscous gravity currents flowing over a porous medium, *J. Fluid Mech.* **622**, 135 (2009).
- [30] R. Sayag and J. A. Neufeld, Propagation of viscous currents on a porous substrate with finite capillary entry pressure, *J. Fluid Mech.* **801**, 65 (2016).
- [31] Y. Liu, Z. Zheng, and H. A. Stone, The influence of capillary effects on the drainage of a viscous gravity current into a deep porous medium, *J. Fluid Mech.* **817**, 514 (2017).
- [32] H. E. Huppert, The propagation of two-dimensional and axisymmetric viscous gravity currents over a rigid horizontal surface, *J. Fluid Mech.* **121**, 43 (1982).
- [33] J. Bear, *Dynamics of Fluids in Porous Media* (Dover, New York, 1988).
- [34] Z. Zheng, S. Shin, and H. A. Stone, Converging gravity currents over a permeable substrate, *J. Fluid Mech.* **778**, 669 (2015).
- [35] J. D. Murray, *Mathematical Biology* (Springer, Berlin, 1989).
- [36] C. W. MacMinn and R. Juanes, Buoyant currents arrested by convective dissolution, *Geophys. Res. Lett.* **40**, 2017 (2013).
- [37] S. Pacala and R. Socolow, Stabilization wedges: Solving the climate problem for the next 50 years with current technologies, *Science* **305**, 968 (2004).
- [38] B. Metz, O. Davidson, H. de Coninck, M. Loos, and L. Meyer, *PICC Special Report on Carbon Dioxide Capture and Storage* (Cambridge University Press, New York, 2005).
- [39] K. C. Meng, R. H. Williams, and M. A. Celia, Opportunities for low-cost CO₂ storage demonstration projects in China, *Energy Policy* **35**, 2368 (2007).
- [40] Z. Zheng, E. D. Larson, Z. Li, G. Liu, and R. H. Williams, Near-term mega-scale CO₂ capture and storage demonstration opportunities in China, *Energy Envir. Sci.* **3**, 1153 (2010).
- [41] J. M. Bielicki, Integrated systems analysis and technological findings for carbon capture and storage deployment, Ph.D. thesis, Harvard University, 2009.
- [42] Z. Zheng, D. Gao, L. Ma, Z. Li, and W. Ni, CO₂ capture and sequestration source-sink match optimization in Jing-Jin-Ji region of China, *Front. Energy Power Eng. China* **3**, 359 (2009).
- [43] L. R. Cowton, J. A. Neufeld, N. J. White, M. J Bickle, J. C White, and R. A. Chadwick, An inverse method for estimating thickness and volume with time of a thin CO₂-filled layer at the Sleipner Field, North Sea, *J. Geophys. Res. Solid Earth* **12**, 5068 (2016).
- [44] M. J. Bickle, Geological carbon storage, *Nat. Geosci.* **2**, 815 (2009).
- [45] M. Bickle, A. Chadwick, H. E. Huppert, M. Hallworth, and S. Lyle, Modelling carbon dioxide accumulation at Sleipner: Implications for underground carbon storage, *Earth Planet. Sci. Lett.* **255**, 164 (2007).
- [46] F. C. Boait, N. J. White, M. J. Bickle, R. A. Chadwick, J. A. Neufeld, and H. E. Huppert, Spatial and temporal evolution of injected CO₂ at the Sleipner field, North Sea, *J. Geophys. Res. Solid Earth* **117**, B03309 (2012).
- [47] J. M. Nordbotten, M. A. Celia, S. Bachu, and H. K. Dahle, Semianalytical solution for CO₂ leakage through an abandoned well, *Environ. Sci. Technol.* **39**, 602 (2005).
- [48] J. Schneider, Compression and permeability behavior of natural mudstones, Ph.D. thesis, The University of Texas at Austin, 2011.
- [49] C. A. Griffith, Physical characteristics of caprock formations used for geological storage of CO₂ and the impact of uncertainty in fracture properties in CO₂ transport through fractured caprocks, Ph.D. thesis, Carnegie Mellon University, 2012.